Three-dimensional chromatin landscapes in T-cell acute lymphoblastic leukemia

Supplementary Notes

Unsupervised clustering of Hi-C data

From our RNA-Seq integration with unsupervised clustering of Hi-C insulation hic-ratio scores, we found that the sample from cluster 2 that did not overlap with canonical T-ALL displayed intermediate expression of both signatures. This T-ALL sample lacked canonical NOTCH1 mutation but harbored activating mutation in Interleukin 7 receptor alpha chain (*IL7R*) [1,2] and deletion of *PTEN* [3] **(Table S2)**.

Compartment shift

Using the c-score tool [4] , we determined compartment scores and integrated H3K27ac ChIP-Seq data for cell lines CUTLL1 (T-ALL), Loucy (ETP-ALL) as well as T cells to assign active (A) and inactive (B) compartments. PCA on genome-wide compartment scores showed a similar separation of T cells, T-ALL and ETP-ALL **(Extended Data 1C)** as observed before with the genome-wide insulation scores.

Super-enhancer calling

Cell-type specific super-enhancers for T cells and T-ALL (using the cell-line CUTLL1) were identified with the ROSE algorithm [5] applied on H3K27ac ChIP-Seq data.

Effect of genomic alterations in TAD activity

Because cancer genomes often show genomic alterations, including inter-chromosomal translocations and copy-number variants (CNVs), we investigated the impact of such events on our intra-TAD activity analysis. First, we have used Hi-C data to identify genome-wide translocation events using HiC-breakfinder [6]. We found that among all identified breakpoints, very few fall within our reported differentially active TADs (**Supplementary Figure 1B**). To map genetic alterations more precisely, we performed whole-genome sequencing in three selected T-ALL samples and called CNVs and tandem-duplications genome-wide. We

overlapped CNVs (separated by gain/loss vs the linear genome) and tandem duplications with increased/decreased intra-TAD activity, respectively. We found that CNV/tandem duplication rarely occur within reported differentially active TADs (**Supplementary Figure 1C**). Furthermore, only two CNV/tandem duplication from two different patients occurred within the TAD boundary adjacent to a differentially active TAD (**Supplementary Figure 1D**). Also, we sought to see whether single nucleotide variants (SNVs) detected from WGS are enriched in any differential TAD-activity category. We did not find a significant enrichment of SNVs in TADs with either increased or decreased activity when compared to SNV occurrences within stably active TADs (**Supplementary Figure 1E**). Thus, we conclude that our analysis is not impacted to a high degree by CNVs or SNVs, suggesting that the majority of 3D chromatin differences reported are regulated epigenetically.

Intra-TAD activity distinguishes between T-ALL subtypes

To investigate subtype specific differences in TAD activity, we evaluated the intra-TAD differences between the canonical T-ALL and ETP-ALL samples. We performed both individual comparisons of T-ALL and ETP-ALL versus T cells, and also directly compared the intra-TAD activity between T-ALL and ETP-ALL. These comparisons identified both common changes in T-ALL and ETP-ALL when compared to T cells, but also disease-specific alterations that reflect both the common lineage and different stages of maturation arrest of the two subtypes **(Extended Data 3A, B)**. Integration of gene expression changes with differentially active TADs again indicated significant correlations of intra-TAD activity changes with expression changes between ETP-ALL and T cells **(Extended Data 3C)**. Similarly, we found a significant correlation of expression changes with intra-TAD activity changes between ETP-ALL and canonical T-ALL **(Extended Data 3D)**, highlighting the impact of 3D architecture on gene expression changes between T-ALL subtypes.

Effect of genomic alterations on TAD boundary changes

Using WGS data, we found only few TAD boundaries displaying increased/decreased insulation capacity in T-ALL overlapping with either genomic deletions or insertions, however, none of the indels directly overlapped with CTCF binding motifs of differential CTCF binding sites (**Extended Data 4A**). We furthermore identified four genomic inversions (potentially leading to aberrant CTCF orientation as previously reported [7,8]) that were found within a range of 100kb to

our reported TAD boundary insulation alterations (**Extended Data 4B**). However, none of them affected genomic loci that contain genes with known functions in T-ALL. Finally, translocation breakpoints were rarely found around our reported TAD boundary alterations, suggesting a potential epigenetic mechanism of regulation for the majority of TAD boundary alterations (**Extended Data 4C**).

Deletion of CTCF boundary in T cells

To confirm the CTCF-mediated insulation of the *MYC* TAD in T cells, we disrupted the CTCF binding site in normal T cells using CRISPR (clustered regularly interspaced short palindromic repeats) mutation **(Extended Data 7A)**. We achieved ~92% of cells harboring indels of varying sizes located within the CTCF motif **(Extended Data 7B)**. Mutations of the CTCF motif in T cells resulted in significantly decreased CTCF binding in the edited T cells **(Extended Data 7C)** and marginally increased MYC expression (**Extended Data 7D**). The decreased binding of CTCF was accompanied by significantly reduced interactions between the *MYC* promoter and the CTCF bound TAD boundary region in edited T cells compared to WT T cells **(Extended Data 7E)**.

γSI insensitive loops bound by dynamic NOTCH1

Our analysis revealed that a subset of dynamic NOTCH1-regulated loci was not associated with either significant H3K27ac loss or reduced long-range chromatin interactions following γSI treatment. Based on this observation, we classified enhancers with reduced NOTCH1 binding and H3K27ac levels upon γSI treatment as γSI-sensitive enhancers, and enhancers with only reduced NOTCH1 binding as γSI-insensitive enhancers **(Extended Data 8F)**. Interestingly, γSI-sensitive enhancers tend to be shorter in length than γSI-insensitive enhancers (**Extended Data 8G**). For example, 4C-Seq analysis detected no significant decrease in the frequency of interactions between the *MYC* promoter and all of the three super-enhancer clusters following γSI treatment **(Extended Data 9A, B)**, although γSI treatment reduced *MYC* expression (**Extended Data 9B, C**) and NOTCH1 binding at the *MYC* super-enhancer (**Extended Data 9A, B**). We also noticed only moderate changes in the H3K27ac distribution within the NOTCH1-bound enhancer elements after γSI treatment **(Extended Data 9A, B)**. Also, the critical CTCF binding within the TAD boundary of MYC was not restored upon γSI treatment **(Extended Data 9D)**. Thus, despite the downregulated MYC mRNA expression and the loss of NOTCH1

binding, pharmacological inhibition of NOTCH1 signaling was not able to significantly alter 3D interactions in this locus. As an additional example, a dynamic NOTCH1-bound enhancer looping to the *IKZF2* promoter did not lose interactions following γSI treatment **(Extended Data 9E, F)**, suggesting that NOTCH1 binding is critical for maintaining enhancer-promoter contacts in only a subset of such loops and additional chromatin regulators may play a role in maintaining chromatin interactions of the γSI-insensitive loops.

4C-Seq validation of THZ1 sensitive loops

The effect of CDK7 inhibition by THZ1 on reducing the *MYC* enhancer-promoter interactions was also conserved in the Jurkat T-ALL cell line **(Extended Data 10E, F)**. Furthermore, loss of both enhancer activity and enhancer-promoter interaction following CDK7 inhibition was also observed in the *IKZF2* locus as shown by the H3K27ac ChIP-Seq data and 4C-Seq in CUTLL1 cells **(Figure 6E, Extended Data 10G)**.

T cell donor Information

	Age (Years)	Sex
T cell donor	60	Male
T cell donor	41	Male
T cell donor	63	Male
T cell donor	38	Male
T cell donor	19	Male
T cell donor	60	Male

Supplementary Methods

ChIP-Seq

ChIP-seq was performed as described previously [9]. All H3K27ac ChIP-Seq experiments were performed in biological duplicates. CTCF ChIP-Seq experiments for primary samples were performed as biological duplicates. For cell line experiments, we performed five replicates for CUTLL1, three replicates for CUTLL1 γSI experiments and two replicates for CUTLL1 JQ1. For all we created a single input sample. In brief, 5 million cells were fixed in 1% formaldehyde and snap frozen in liquid nitrogen and stored in -80 °C till usage. For Histone chips, 2 million cells were crosslinked as previously described. Nuclei were isolated from the fixed cells using the nuclei isolation buffer (15mM Tris pH 7.5, 60mM KCl, 15mM NaCl, 15mM MgCl2, 1mMCaCl2, 250 mM Sucrose, 1mM DTT and Protease inhibitor). The isolated nuclei were lysed using nuclei lysis buffer (50 mM Tris-HCl (pH 8.0), 10 mM EDTA (pH 8.0) and 1% SDS). This was followed by sonication (30 mins in total) using the bioruptor from Diagenode at high output with 30s ON and 30s OFF cycles. Following sonication to the desired fragment size of 400-600 bp, the sonicated lysate was diluted with nine volumes of IP dilution buffer (0.01% SDS, 1.1% Triton X-100, 1.2 mM EDTA (pH 8.0), 16.7 mM Tris-HCl pH 8.0 and 167 mM NaCl) and magnetic DynaI beads for 1h (preclearing of chromatin). Following preclearing, CTCF was immunoprecipitated with 10 µl of monoclonal rabbit CTCF antibody, clone D31H2 (Cell Signaling 3418) overnight at 4 °C or H3K27ac (Active motif; Catalog no: 39133). The purified ChiP DNA was used to generate sequencing libraries using Hapa Hyper prep kit from Kapa Biosystems. Libraries were sequenced in single-end using Illumina Hiseq 2500 or Illumina Hi-seq 4000 at 50 cycles.

RNA-Seq

RNA-seq libraries were prepared using NEXTflex Rapid Illumina Directional RNA-seq Library prep kit as per manufacturer's guidelines. The libraries were sequenced in single-end by either HiSeq 2500 or HiSeq 4000 at 50 cycles.

qPCR

RNA was extracted using the RNeasy Mini Kit using Qiagen kit (Catalog no: 74106) following manufacturer's guidelines. cDNA was generated using High Capacity RNA-to-cDNA kit from Life Technologies (Catalog no: 4387406) following manufacturer's guidelines. cDNA was used to perform qPCR using Light cycler 480 SYBR green I Master Mix from Roche Diagnostics (Catalog no: 04887352001). See Supplementary Table for primer sequences. The reactions were run in Roche Light cycler 480 II.

Immunoblotting

CUTLL1 cells treated with DMSO, γSI or THZ1 were pelleted and lysed using RIPA lysis and extraction buffer (Thermo Fisher, Catolog no: 89900). The lysates were boiled with Laemmli buffer, resolved by SDS-PAGE, transferred to PVDF membranes and proteins visualized by immunoblotting. c-MYC (D84C12) rabbit monoclonal antibody was purchased from Cell signaling and anti-actin antibody was purchased from Millipore (Catalog no. MAB1501R)

3D FISH quantification of MYC enhancer-promoter distances

To quantify enhancer-promoter distances from DNA FISH data, we first used AirLocalize (Lionnet et al, Nature Methods 2011) to automatically detect spots in enhancer and promoter channels and estimated their position with subpixel resolution. For enhancers (red channel), the detection parameters were set to $\sigma xy = 2.4621$, $\sigma z = 1.1768$ pixels and the intensity threshold to 5000 counts (typical voxel sizes: 73 nm in xy, 360 nm in z). For promoters (green channel), the detection parameters were set to $\sigma xy = 2.8801$, $\sigma z = 1.1776$ pixels and the intensity threshold to 4000 counts. Then we filtered the spots by eliminating spots located outside the nucleus or with integrated intensity lower than 1.5e6 counts in red or 0.75e6 counts in green. Next, we computed and plotted the histograms of the distance matrix between spots in the red and green channels. For a perfectly aligned and corrected system, the means of the dx, dy and dz histograms should be 0 in all three directions for there is no reason for enhancers to prefer one relative orientation to promoters than others. We therefore corrected the offsets of the two channels by subtracting the means of the dx, dy and dz histograms from individual coordinate differences. After correction, we computed the distance matrix again. In the distance matrix, we found pairs of spots that are the nearest neighbors to each other, mutual nearest neighbors, which we defined as pairs of

enhancers and promoters and built the matrix of their distances. Finally, we plotted cumulative probability distributions of enhancer-promoter distances in the different conditions (N = 30, 23 and 16 image stacks for the CUTTL1-DMSO, CUTTL1-THZ1 and T cells respectively; a typical image contains 10-20 nuclei; probe-pairs T cells = 993, probe-pairs CUTLL1 DMSO = 2001, probe-pairs CUTLL1 THZ1 = 1308). Results were robust to changes in bin size, subsets of images analyzed, or slight changes in imaging conditions, or considering all nearest neighbors rather than only mutual nearest neighbors. Significance for differential co-localization was derived using a Kolmogorov-Smirnow test.

Bioinformatics analysis:

Hi-C analysis

In-situ Hi-C datasets were analyzed with the HiC-bench platform[10]. In short, both datatypes were aligned against the human reference genome (GRCh37/hg19) by bowtie2 (version 2.3.1)[11] with mostly default parameters (specific settings: --very-sensitive-local --local). For Hi-C, aligned reads were filtered by the GenomicTools[12] tools-hic filter command (integrated in HiC-bench), which discards multi-mapped reads ("multihit"), read-pairs with only one mappable read ("single sided"), duplicated read-pairs ("ds.duplicate"), read-pairs with a low mapping quality of MAPQ < 20, read-pairs resulting from self-ligated fragments (together called "ds.filtered") and short-range interactions resulting from read-pairs aligning within 25kb ("ds.too.short"). The reads used for downstream analyses are all accepted intra-chromosomal read-pairs ("ds.accecpted intra"), which were consistently above 25% across all Hi-C samples. The absolute number of accepted intra-chromosomal read-pairs varied between ~40 and ~120 million. Interaction matrices for each chromosome separately were created by the HiC-bench platform at 40kb resolution. Filtered read counts were normalized by a method called "iterative correction and eigenvector decomposition" (ICE) [13]. To account for variances of read counts of more distant loci, which tend to be less covered the further distant the interacting loci are apart in the genome, we performed distance normalization for each chromosome matrix as recently described [14].

TADs were called using the algorithm developed within hic-bench [10] setting the insulating window to 500kb (**Table S5**). The matrix-wide stratum-adjusted correlation score (SCC) was calculated using HiC-Rep [15] for each possible pair-wise comparisons of all 13 Hi-C samples. The SCC was first calculated for each pair of chromosome matrices for any possible pair-wise

comparison. The final score for a sample-comparison was calculated as the average of all its chromosome scores. Principal Component Analysis (PCA) on Hi-C datasets was performed in R (prcomp, with scale=TRUE and center=TRUE) using the genome-wide Hi-C "ratio" insulation scores for 500kb windows, as defined in Lazaris et al. [10]. Unsupervised clustering on hic-ratio insulation scores was performed using the R package Mclust version 5.3 (https://cran.r-project.org/web/packages/mclust/index.html), and both EII and VII models found three clusters to be the optimal separation of samples. For visualization of Hi-C data, we created heatmaps for regions of interest using the normalized contact matrices. Heatmaps were generated with the R function image, and color scale was set to the highest normalized score seen in any sample for the particular window. Fold-change heatmaps were generated by calculating the log2 fold-change for each matrix bin vs. T cell 1 sample.

CTCF & H3K27ac ChIP-Seq analysis

ChIP-Seq datasets were analyzed with the HiC-bench platform [10]. The ChIP-Seq aligned reads were further filtered by discarding reads with low mapping quality (MAPQ < 20) and duplicated reads using picard-tools (https://github.com/broadinstitute/picard). The remaining reads were analyzed by applying the peak-calling algorithm MACS2 (version 2.0.1) [16] with input as control (option -c) wherever applicable. Binding of transcription factor CTCF was determined from narrow-peak calls, while histone-marks were determined from broad-peak calls (option --broad). For differential binding affinity analysis, we ran the R Bioconductor package diffBind with default parameters, which outputs p-value, false-discovery rate and fold-changes of binding affinity for all identified peaks from either sample of any possible pair-wise comparison. For normalization during diffBind, we used the option "method=DBA_EDGER". For visualization, we generated bigwig tracks (with the help of bedtools version 2.27.1) as fold-enrichment combining all replicates of the actual sample over input wherever applicable using the MACS2 bdgcmp function (with "-m FE"). All bigwig tracks shown were created with IGV (version 2.3.83). CTCF orientation for canonical CTCF binding sites depicted in all tracks with CTCF ChIP-Seq was generated by PWMScan [17] (database JASPAR CORE vertebrates; filtered by p-value < 1E-5). Differential binding heatmaps and peak signal quantification were generated with deeptools (version 2.3.3) [18] and visualized the 2.5kb up- and downstream of the peak-summit.

RNA-Seq

RNA-Seq reads were aligned against the human reference genome (GRCh37/hg19) using the STAR aligner (version 2.5.0c)[19] with default parameters, discarding all non-uniquely aligned reads. Duplicated reads were discarded using picard-tools. For read counting per gene, we used bamutils count of the ngsutils package (version 0.5.7)[20] on gene annotations from Ensembl V75 in a stranded manner (options -uniq -multiple complete -library RF). Downstream processing was performed in R with the Bioconductor package edgeR (version 3.14.0)[21] on stranded gene counts, normalizing for intra- and inter-sample variances (edgeR functions calcNormFactors and estimateTagwiseDisp), resulting in counts-per million (CPM) per annotated gene. For cell line data with multiple replicates (CUTLL1 n=3, Jurkat n=2), CPM values were averaged. Differential expression analysis was performed per condition (leukemia vs. normal T cells) with edgeR functions glmQLFit and glmQLFTest.

GRO-Seq

GRO-Seq reads were aligned against the human reference sequence GRCh37/hg19 using bowtie (version 1.0.0)[11]. All aligned reads were filtered for unique alignment positions (MAPQ > 20). Next, the remaining reads were counted in a stranded manner per annotated gene in Ensembl Genes V75 using bamutils count of the ngsutils package (version 0.5.7; options -uniq -multiple complete -library RF)[20]. We performed normalization using edgeR[21] (version 3.14.0; functions calcNormFactors and estimateTagwiseDisp), resulting in counts per millions (CPM) per gene followed by averaging data from replicates. For visualization, we created bigwig tracks per genomic strand using bedtools coverage (2.27.1) after normalizing for sequencing depth and fragment length of 250bp (bedtools coverage option -fs 250). All tracks were visualized with IGV (version 2.3.83).

4C-Seq

4C-Seq reads were processed similarly as described in [22,23]. First, a reduced genome reference was created for the human reference genome (GRCh37/hg19) by only considering unique sequence fragments from the reference genome sequence that are adjacent to the restriction sites of the restriction enzyme (DpnII) used during the 4C protocol (following the 4C-ker pipeline [22]). All reads were aligned against this reduced genome reference by bowtie (version 1.0.0) [11], only

considering uniquely aligned reads. All self-ligated and undigested fragments were removed (following the 4C-ker pipeline). We further validated that all samples had > 0.5 million mapped reads and > 0.5 cis/trans ratio of mapped reads [23]. Next, we defined successive overlapping windows of different resolutions (10kb and 40kb), and all adjacent windows are overlapping by 90% of their length (9kb and 36kb respectively). We counted uniquely mapped reads for each window per sample and performed normalization with edgeR (leading to CPM per window). This accomplishes a smoothed signal across samples for different sizes of regions to be plotted (approx. 300kb in Figures 5E, 5F, S10E and 6E using 10kb resolution and ~2MB in Figures 4C, S7, S8E, S10A, 6D and S11E using 40kb resolution). Data from biological replicates were averaged after normalization for visualization. Differential interactions were identified with edgeR (version 3.14.0) functions glmQLFit and glmQLFTest, and log10(p-value) is shown on the negative y-axis of all 4C plots as indicator for the most significant changes. We have not performed multiple testing correction, as each data-point is dependent due to overlapping windows, and would thus potentially lead to a too stringent correction. Quantifications were calculated for the highest single peak (at 10kb resolution for LUNAR1, APCDD1, IKZF2; at 40kb resolution for MYC) within depicted enhancers/promoters in the respective Figures by grey boxes. Normalized 4C signals, as calculated by cpm-function within edgeR, were further normalized against the average control replicates, and shown in percent. Specific p-values shown in Figures were also taken for the same 10kb/40kb bin showing highest 4C signal within respective enhancer/promoter.

Compartment analysis and RNA-Seq integration

Compartment calling was performed using the filtered Hi-C reads of the hic-bench pipeline for all 13 Hi-C samples individually. The "c-score tool" [4] was used to determine the A and B compartments at 100kb windows, using information on active chromatin from H3K27ac ChIP-Seq in T cells, CUTLL1 (for T-ALL) and Loucy (for ETP-ALL) to assign A/B to resulting compartment scores. Windows with missing c-score values for at least one sample are removed from the analysis. P-values were calculated using an unpaired two-sided t-test to determine the statistical significance of compartment shifts for the following comparisons: T-ALL vs T cells, ETP-ALL vs T cells and ETP-ALL vs T-ALL samples. After p-value calculation, the mean c-score for all T-ALL, all ETP-TALL and all T cell samples were calculated. Compartment shifts

were determined as “A to A” when the mean c-score values for both conditions are > 0.1, “B to B” shift if the mean c-score value for both conditions is < -0.1, and “A to B”/”B to A” shift if the mean c-score value of one condition is < -0.1 and > 0.1 for the other condition (p-value < 0.1).
Unique compartment shifts for either T-ALL or ETP-ALL were identified by combining the results of the above three comparisons. More specifically, an “A to B” shift is considered T-ALL specific if it is identified as an “A to B” shift in the T-ALL vs T cell comparison, but as a “B to A” event in the ETP-ALL vs T-ALL comparison. A “B to A” shift is considered T-ALL specific when it is identified as a “B to A” shift in the T-ALL vs T cell comparison, but as an “A to B” shift for the ETP-ALL vs T-ALL comparison. Similarly, an “A to B” shift is ETP-ALL specific, when it is found as an “A to B” shift for the ETP-ALL vs T cell comparison and an “A to B” shift in the ETP-ALL vs T-ALL comparison; a “B to A” shift is ETP-ALL specific when it is identified as a “B to A” shift in both ETP-ALL vs T cell and ETP-ALL vs T-ALL comparisons.
Genes (Ensembl V75 annotations; only protein-coding, processed transcripts and lincRNAs with FPKM > 1) were integrated if their promoters were falling within a respective compartment bin. For each gene, we took the log2 FC from the edgeR output for the respective comparison (T cell vs T-ALL or ETP-ALL vs T-ALL). Significance in global changes of RNA expression was calculated as a one-sided t-test on logFCs from each differential group (i.e. A to B or B to A shifts) vs. A to A compartments, following the hypothesis of a positive correlation between gene expression and compartment assignment.

Differential TAD activity and data integration

To identify TADs of differential intra-TAD activity, we developed an algorithm to detect statistically significant overall changes between samples of any two conditions (e.g. T-ALL vs. T cells). Firstly, we identified TADs that are common in both conditions. This was done by only considering TADs whose boundaries on either side of the TAD are as close as three bins between the two samples (i.e. 120kb in a 40kb resolution), setting the boundaries of the common TAD to those which yield the largest TAD. We also set a minimum TAD length to 10 bins (400kb). We further removed TADs that fall in the B compartment in both conditions by at least 75% of the genomic TAD area, to avoid minor changes in TAD activity within highly repressed chromatin. This set of common TADs between any two conditions c_1 and c_2 is denoted as T. For each interaction bin, we averaged the Hi-C matrix score across conditions (i.e. all T cell, T-ALL or

ETP-ALL samples). Next, we performed a paired two-sided t-test on each single interaction bin within each common TAD between the average Hi-C matrix values per condition and calculated the log2 fold-change between the average scores of all interaction intensities within such TADs between the two samples:

$$TAD\ activity\ change(t) = log2(\left(\frac{\sum_{i \in I_t} c_{2_i}}{\#I_t}\right) / \left(\frac{\sum_{i \in I_t} c_{1_i}}{\#I_t}\right))$$

for each $t \in T$, and I_t being all intra-TAD interactions for TAD t.

We also applied multiple testing correction by calculating the false-discovery rate per common TAD (using the R function p.adjust with method="fdr"). For downstream analyses, we filtered common TADs as differentially active by setting the FDR < 0.1 and absolute log2 fold-change > 0.58. As a negative control group, we defined stable TADs of stable high activity by filtering for TADs with an absolute log2 fold-change < 0.1 and average TAD activity within the top 50% quantile of all TAD activity scores. For downstream CTCF occupancy integration, we extended the TAD boundary for each such identified TAD by 2 bins (80kb) on either side of the boundary accounting for false boundary calls. Changes in CTCF occupancy within these boundaries were defined as the sum of all their log2 FCs taken from the diffBind output, matching the equivalent comparison of T cells vs. T-ALL. Significant changes in global CTCF occupancy within such boundaries were calculated using a one-sided t-test on logFCs from each group (i.e. higher or lower activity in leukemia samples) vs. stable TADs, following the hypothesis of a positive correlation between CTCF binding and TAD boundary strength / TAD activity as recently reported [24]. Genes (Ensembl V75 annotations; only protein-coding, processed transcripts and lincRNAs with FPKM > 1) were integrated if their promoters were falling within the TADs, extending each TAD by 2 bins (80kb) to either side accounting for inaccurate boundary calls. For each gene, we took the log2 FC from the edgeR output for the respective comparison (T cell vs T-ALL or ETP-ALL vs T-ALL). Significance in global changes of RNA expression was calculated as a one-sided t-test on logFCs from each group (i.e. higher or lower activity in leukemia samples) vs. stable TADs, following the hypothesis of a positive correlation between TAD activity and gene expression. Lastly, dynamic NOTCH1-binding sites taken from Wang et al. [25] were overlapped with TADs of stable or differential activity using bedtools and a minimum overlap of 1bp, and normalized to 1Mb in order to account for different TAD sizes. Significant

differences between categories of stable / differential TAD activity was performed using an unpaired two-sided t-test.

Super-enhancer calling and integration

For T cell and CUTLL1 H3K27ac ChIP-Seq data, we applied our standard ChIP-Seq analysis pipeline (https://github.com/NYU-BFX/hic-bench), as described above in detail. Next, we ran ROSE [5] with default parameters to define super-enhancers. For each dataset, we have excluded common super-enhancers defined as super-enhancers from both cell-types overlapping by at least 1bp on the genomic coordinates in order to define cell-type specific super-enhancers. We overlapped the remaining cell-type specific super-enhancers with differential active TADs if the overlapping genomic coordinates were larger than 1bp. Enrichment score ES of super-enhancers defined as observed over expected overlap was calculated as follows:

$$ES = \frac{OV}{\frac{DA\_TADs * SE\_TADs}{T}}$$

with SE_TADs being all TADs containing at least one super-enhancer, DA_TADs being all differentially active TADs, OV being the intersection of SE_TADs and DA_TADs and T being all TADs the analysis was performed on. Statistically significant enrichment against background (SE_TADs) was determined using a two-sided Fisher exact test.

Compartment shifts within differentially active TADs

We have overlapped compartment information with the differentially active TADs for the T-ALL vs T cell comparison to determine potential compartment shifts within the genomic area of each TAD. Therefore, we have defined “A to B”, “B to A”, “A to A” and “B to B” shifts as described above. To this end, the length of each TAD was determined and the numbers of compartment shifts from any of the previous categories overlapping each TAD were calculated. Then, the percentage of overlap for each TAD was calculated regarding the four compartment shift categories and the average overlap of each category across all TAD categories is shown.

TAD boundary insulation alterations and differential CTCF integration

We sought to detect more complex changes in chromatin architecture by defining TAD boundary insulation alterations. We separated those into losses and gains of TAD boundaries between

normal T cells and leukemia (as depicted in Figure 3A). The analysis was performed in a two-step approach, differentiating between TAD boundary loss and TAD boundary gain as changes resulting from lost versus novel TAD boundaries from the perspective of the leukemia samples, respectively. We thus performed the analysis of identifying insulation changes based on adjacent T cell TADs (yielding TAD boundary losses) and *vice versa* on adjacent leukemia TADs (yielding TAD boundary gains). Thus, for each pair of adjacent TADs for either T cell or T-ALL TAD calls, we determined the interaction strengths of all inter-TAD interactions and intra-TAD interactions for both the two adjacent TADs. The TAD boundary insulation alteration score BIC for each pair of adjacent TADs was calculated as $BIC = inter\text{-}TAD\ interactions * max(intra\text{-}TAD\ interactions)$. To select the strongest outliers of this analysis as TAD boundary alterations, we took the top 5% quantile of all BIC scores between T-ALL and normal T cells. To determine whether these outliers are significant, we performed the same analysis between all three normal T cell donors, applying the same threshold taken from the T cell vs. T-ALL comparison, assuming that there are no severe TAD boundary alterations between any two normal controls. This yielded on average 12 (TAD boundary loss) and 17 (TAD boundary gain) outliers for all three pair-wise comparisons of normal controls, thus we achieved controlling for an average FDR ~10.77% in T cells vs. T-ALL under the assumption of no boundary insulation changes between normal T cells. For interesting loci, we manually integrated CTCF occupancy and RNA expression changes.

Genome-wide detection of enhancer activity changes in γSI/THZ1 treated samples

All detected H3K27ac peaks from ChIP-Seq were first overlaid with promoters of annotated genes taken from Ensembl Genes V75. All peaks with a distance of more than 1kb from an annotated promoter (measured from the peak-boundaries) were considered enhancers. Then, we created sets of stable/constant, loss and gain of enhancers in CUTLL1 after γSI or THZ1 treatment using diffBind [26] on H3K27ac ChIP-Seq. For stable enhancers, we filtered all peaks with abs(logFC) < 0.2; for reduced/loss of enhancer activity, we filtered all peaks with logFC < -1.0 / > 1.0 and FDR < 0.05. For γSI-treatment data, we further overlapped all three groups with dynamic NOTCH1-binding sites taken from Wang et al.[25]. Enrichment scores (observed over expected) were calculated similarly as described above, using a two-sided Fisher's exact test for significance calculation.

Differential binding analysis using LOLA

In order to define potential co-factors of enhancer/looping activity in γSI-sensitive and insensitive enhancers (Suppl. Figure 9F), we used LOLA [27]. To this end, we downloaded the LOLA database (http://databio.org/regiondb) and kept ChIP-Seq data from T-ALL related cell lines (Jurkat, CUTLL1 or HPB-ALL), that displayed at least 3000 peaks. We are representing the results as percent overlap between ChIP-Seq peaks and γSI-sensitive / insensitive genomic locations. Statistics for differences between γSI-sensitive and insensitive enhancers was calculated using a two-sided Fisher exact test.

HiChIP data analysis and loop calling

H3K27ac HiChIP data in CUTLL1 was processed with the hic-bench platform similarly as described above for Hi-C data. We have used output of filtered/accepted intra-chromosomal reads, and performed mango [28] to identify significant loops at a 40kb resolution. The trajectories of each matrix bin of the HiChIP data onto both anchors on the diagonal were overlaid with peaks identified from H3K27ac ChIP-Seq in CUTLL1, requiring a minimal overlap of 1bp between a HiChIP-bin and a ChIP-peak. Only loops that were supported by a ChIP-peak in at least one anchor were kept for further analyses. We then applied sequencing-depth normalization (CPM) per replicate followed by a statistical approach described in mango, which employs a binomial test in each diagonal of the counts-matrix up to a maximum distance of 2Mb. High-confidence HiChIP loops were identified by FDR < 0.1 and requiring a minimum CPM > 5 per loop. We have only kept loops that contain an H3K27ac peak outside any annotated promoter in one anchor and an annotated promoter in the other anchor, thus defining promoter-enhancer loops for downstream Hi-C integration analyses.

Hi-C analysis for γSI/THZ1 treated cells using HiChIP defined enhancer-promoter interactions

Next, to investigate the involvement of changes in enhancer H3K27ac signal in nearby gene expression and loop formation upon γSI/THZ1 treatment in CUTLL1, we integrated Hi-C data with promoter-enhancer loops. To this end, we first identified candidate interactions of promoter-enhancer pairs using loop calling from H3K27ac HiChIP data in CUTLL1, as described above. We further took these specific promoter-enhancer pairs and calculated changes in Hi-C

connectivity, using the normalized contact matrices at 40kb resolution. We calculated log2 fold-changes between DMSO and γSI/THZ1 treatment matrices after averaging Hi-C matrices across replicates in each condition. Global loss/gain of interactions upon γSI/THZ1 treatment was depicted by a one-sided t-test comparing all groups vs. the stable H3K27ac group, following the hypothesis of a positive correlation between promoter-enhancer looping and enhancer activity.

Integration of GRO-Seq data with findings from combined H3K27ac ChIP and HiChIP analysis

For all genes connected with nearby differential/stable enhancers (categorized by ChIP-Seq as described above) detected from HiChIP, we investigated expression of such genes before treatment, after treatment and after 1, 2, 3, 4, 5, 6, and 10 hours post drug "wash off". We are representing the median FPKM across all genes (FPKM > 1) of a respective enhancer-promoter loop category per time-point. The genome-wide trend of reduced expression for specific H3K27ac categories was determined by a one-sided t-test comparing expression with all genes within stable H3K27ac enhancer-loops, following the hypothesis of a positive correlation between expression changes and looping/enhancer activity.

WGS analysis and integration with TADs and CTCF binding

Whole-genome sequencing and subsequent data analysis in primary T-ALL samples was performed by GeneWiz (https://www.genewiz.com/). In short, copy number variants were called using Canvas version 1.3.1 and SNVs and SVs were called using Manta version 0.28.0. SNVs were further filtered by applying 1000genomes project "global minor allele frequency" (GMAF) < 1%. Results of CNVs/tandem duplications, other SVs or SNVs were overlapped with genomic areas of (differentially active) TADs or TAD boundaries expanded by 1 bin (40kb) in each direction using bedtools intersect and a minimum overlap of 1bp. Overlap of SVs or SNVs with CTCF binding information was performed by first overlapping differential CTCF peak calls with CTCF motif information derived from PWMScan (database JASPAR CORE vertebrates; filtered by p-value < 1E-5), and then with SVs or SNVs using bedtools intersect and a minimum overlap of 1bp. Significance of overlaps was calculated using two-sided Fisher exact test.

Translocation calling from genome-wide Hi-C data

We have used HiC-breakfinder [6] to identify intra- and inter-chromosomal translocations from all T-ALL Hi-C samples within this study (excluding cell line data with drug treatments). To this end, we have utilized the entire proposed pipeline including BAM-file reformatting according to developers' instructions (https://github.com/dixonlab/hic_breakfinder). Resulting translocations were filtered for a maximum resolution of 100kb and merged if both break-ends were within 1Mb of both break-ends of another translocation to account for inaccurate translocation calling.

Supplementary Figure 1

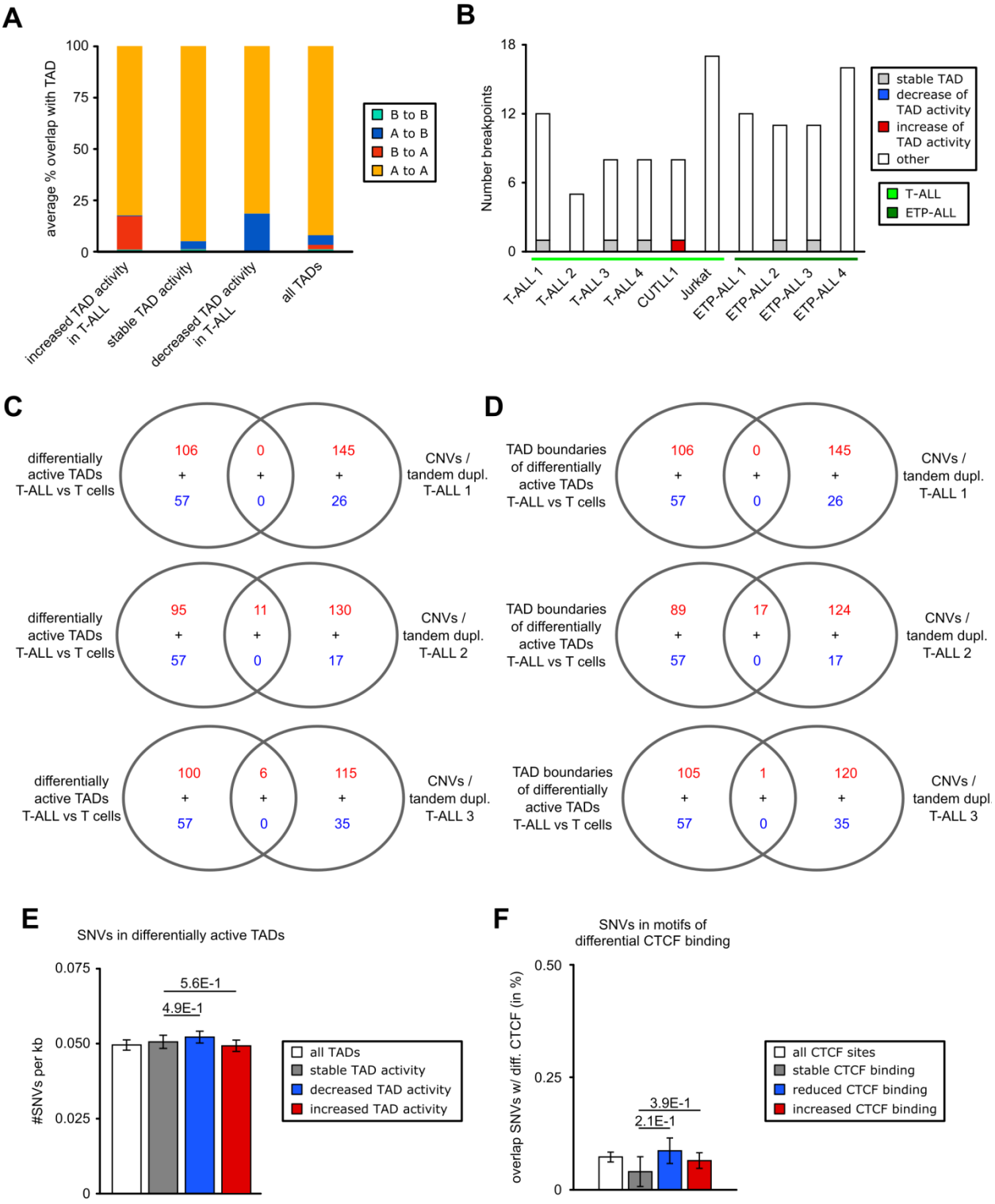

Supplementary Figure S1: A) Average genomic area of TADs (in percent) of differential / stable activity or all TADs overlapping with compartment shifts. Differentially active / stable TADs are defined in Figure 2A; compartment shifts are defined in Figure 1E.

B) Translocations from Hi-C data of T-ALL samples were called using HiC-breakfinder [6]. Unique breakpoints were overlapped with differentially active TADs defined in Figure 2A.

C+D) WGS detected CNVs (gain / loss) and tandem duplication from overlap with differentially active TADs (C) / boundaries of differentially active TADs (D), both defined in Figure 2A. Overlap was performed using bedtools intersect, using 1bp overlap between TAD area (C) / TAD boundary extended by 40kb on each side (D) and CNV/tandem duplication.

E) Integration of SNVs detected from WGS of T-ALL 1, 2 and 3with TAD activity results. SNVs per Megabase (Mb) were counted within genomic areas of all, stably or differentially active TADs. Statistical analysis was performed using two-sided Fisher exact test between numbers of all SNVs overlapping loss/gain of TAD activity and numbers of all SNVs within stably active TADs.

F) Integration of SNVs with CTCF binding motifs within differential CTCF binding genome-wide. Differential CTCF binding between all profiled T-ALL and T cell samples was determined using DiffBind with edgeR-method (FDR < 0.1, log2 fold-change > 1 for increased CTCF binding and log2 fold-change < -1 for decreased CTCF binding in T-ALL; stable CTCF was determined by log2 fold-change > -0.2 and log2 fold-change < 0.2). Statistical analysis was performed using two-sided Fisher exact test between overlap of SNVs with differential CTCF binding and overlap of SNVs with stable CTCF binding.

Supplementary References

1. Shochat, C. *et al.* Gain-of-function mutations in interleukin-7 receptor-alpha (IL7R) in childhood acute lymphoblastic leukemias. *J Exp Med* **208**, 901-8 (2011).
2. Zenatti, P.P. *et al.* Oncogenic IL7R gain-of-function mutations in childhood T-cell acute lymphoblastic leukemia. *Nat Genet* **43**, 932-9 (2011).
3. Gutierrez, A. *et al.* High frequency of PTEN, PI3K, and AKT abnormalities in T-cell acute lymphoblastic leukemia. *Blood* **114**, 647-50 (2009).
4. Zheng, X. & Zheng, Y. CscoreTool: fast Hi-C compartment analysis at high resolution. *Bioinformatics* **34**, 1568-1570 (2018).
5. Whyte, W.A. *et al.* Master transcription factors and mediator establish super-enhancers at key cell identity genes. *Cell* **153**, 307-19 (2013).

6. Dixon, J.R. *et al.* Integrative detection and analysis of structural variation in cancer genomes. *Nature Genetics* **50**, 1388-1398 (2018).
7. de Wit, E. *et al.* CTCF Binding Polarity Determines Chromatin Looping. *Mol Cell* **60**, 676-84 (2015).
8. Guo, Y. *et al.* CRISPR Inversion of CTCF Sites Alters Genome Topology and Enhancer/Promoter Function. *Cell* **162**, 900-10 (2015).
9. Ntziachristos, P. *et al.* Genetic inactivation of the polycomb repressive complex 2 in T cell acute lymphoblastic leukemia. *Nat Med* **18**, 298-303 (2012).
10. Lazaris, C., Kelly, S., Ntziachristos, P., Aifantis, I. & Tsirigos, A. HiC-bench: comprehensive and reproducible Hi-C data analysis designed for parameter exploration and benchmarking. *BMC genomics* **18**, 22 (2017).
11. Langmead, B. & Salzberg, S.L. Fast gapped-read alignment with Bowtie 2. *Nat Methods* **9**, 357-9 (2012).
12. Tsirigos, A., Haiminen, N., Bilal, E. & Utro, F. GenomicTools: a computational platform for developing high-throughput analytics in genomics. *Bioinformatics* **28**, 282-3 (2012).
13. Imakaev, M. *et al.* Iterative correction of Hi-C data reveals hallmarks of chromosome organization. *Nat Meth* **9**, 999-1003 (2012).
14. Gong, Y. *et al.* Stratification of TAD boundaries reveals preferential insulation of super-enhancers by strong boundaries. *Nat Commun* **9**, 542 (2018).
15. Yang, T. *et al.* HiCRep: assessing the reproducibility of Hi-C data using a stratum-adjusted correlation coefficient. *Genome Research* **27**, 1939-1949 (2017).
16. Zhang, Y. *et al.* Model-based analysis of ChIP-Seq (MACS). *Genome Biol* **9**, R137 (2008).
17. Ambrosini, G., Groux, R. & Bucher, P. PWMScan: a fast tool for scanning entire genomes with a position-specific weight matrix. *Bioinformatics* (2018).
18. Ramirez, F. *et al.* deepTools2: a next generation web server for deep-sequencing data analysis. *Nucleic Acids Res* **44**, W160-5 (2016).
19. Dobin, A. *et al.* STAR: ultrafast universal RNA-seq aligner. *Bioinformatics* **29**, 15-21 (2013).
20. Breese, M.R. & Liu, Y. NGSUtils: a software suite for analyzing and manipulating next-generation sequencing datasets. *Bioinformatics* **29**, 494-6 (2013).

21. Robinson, M.D., McCarthy, D.J. & Smyth, G.K. edgeR: a Bioconductor package for differential expression analysis of digital gene expression data. *Bioinformatics* **26**, 139-40 (2010).
22. Raviram, R. *et al.* 4C-ker: A Method to Reproducibly Identify Genome-Wide Interactions Captured by 4C-Seq Experiments. *PLoS Comput Biol* **12**, e1004780 (2016).
23. Rocha, P.P. *et al.* A Damage-Independent Role for 53BP1 that Impacts Break Order and Igh Architecture during Class Switch Recombination. *Cell Rep* **16**, 48-55 (2016).
24. Gong, Y. *et al.* Stratification of TAD boundaries reveals preferential insulation of super-enhancers by strong boundaries. *Nature Communications* **9**, 542 (2018).
25. Wang, H. *et al.* NOTCH1–RBPJ complexes drive target gene expression through dynamic interactions with superenhancers. *Proceedings of the National Academy of Sciences* **111**, 705-710 (2014).
26. Ross-Innes, C.S. *et al.* Differential oestrogen receptor binding is associated with clinical outcome in breast cancer. *Nature* **481**, 389-93 (2012).
27. Sheffield, N.C. & Bock, C. LOLA: enrichment analysis for genomic region sets and regulatory elements in R and Bioconductor. *Bioinformatics* **32**, 587-589 (2015).
28. Phanstiel, D.H., Boyle, A.P., Heidari, N. & Snyder, M.P. Mango: a bias-correcting ChIA-PET analysis pipeline. *Bioinformatics* **31**, 3092-8 (2015).